

# Structural properties of the Southern San Andreas fault zone in northern Coachella Valley from magnetotelluric imaging

Pieter-Ewald Share<sup>1,†</sup>, Jared R. Peacock,<sup>2</sup> Steven Constable,<sup>1</sup> Frank L. Vernon<sup>1</sup> and Shunguo Wang<sup>3</sup>

<sup>1</sup>Institute of Geophysics and Planetary Physics, University of California San Diego, La Jolla, CA, USA. E-mail: [pieter.share@oregonstate.edu](mailto:pieter.share@oregonstate.edu)

<sup>2</sup>U.S. Geological Survey Geology, Minerals, Energy, and Geophysics Science Center, Moffett Field, CA, USA

<sup>3</sup>Department of Electronic Systems, Norwegian University of Science and Technology, Trondheim, Norway

Accepted 2022 September 6. Received 2022 August 21; in original form 2021 December 13

## SUMMARY

The Southern San Andreas fault (SSAF) poses one of the largest seismic risks in California. Yet, there is much ambiguity regarding its deeper structural properties around Coachella Valley, in large part due to the relative paucity of everyday seismicity. Here, we image a multistranded section of the SSAF using a non-seismic method, namely magnetotelluric (MT) soundings, to help inform depth-dependent fault zone geometry, fluid content and porosity. The acquired MT data and resultant inversion models highlight a conductive column encompassing the SSAF zone that includes a 2–3 km wide vertical to steeply northeast dipping conductor down to ~4 km depth (maximum of ~1 Ω·m at 2 km depth) and another prominent conductor in the ductile crust (~1 Ω·m at 12 km depth and slightly southwest of the surface SSAF). We estimate porosities of 18–44 per cent for the conductive uppermost 500 m, a 10–15 per cent porosity at 2 km depth and that small amounts (0.1–3 per cent) of interconnected hypersaline fluids produce the deeper conductor. Located northeast of this conductive region is mostly resistive crust indicating dry crystalline rock that extends down to ~20 km in places. Most of the local seismicity is associated with this resistive region. Located farther northeast still is a conductive region at >13 km depth and separate from the one to the southwest. The imaged anomalies permit two interpretations. The SSAF zone is vertical to steeply northeast dipping in the upper crust and (1) is near vertical at greater depth creating mostly an impermeable barrier for northeast fluid migration or (2) continues to dip northeast but is relatively dry and resistive up to ~13 km depth where it manifests as a secondary deep ductile crustal conductor. Taken together with existing knowledge, the first interpretation is more likely but more MT investigations are required.

**Key words:** Electrical properties; Magnetotellurics; Continental tectonics: strike-slip and transform; Fractures, faults, and high strain deformation zones.

## 1 INTRODUCTION

The Southern San Andreas Fault (SSAF) has not produced a  $M > 7.5$  event for > 300 yr but is estimated to pose one of the largest seismic risks in California (Sieh & Williams 1990; Weldon *et al.* 2005). Several properties of the SSAF such as fault zone damage, geometry and fluid content remain poorly understood despite several geoscientific studies (e.g. Catchings *et al.* 2009; Lindsey & Fialko 2013; Ajala *et al.* 2019). Informing these properties is essential as they may play key roles in the magnitude and subsequent shaking

from future large events (e.g. Fialko 2006; Roten *et al.* 2015; Biasi & Wesnousky 2016).

One outstanding question is whether the SSAF at depth, if well localized as expected for a mature plate margin (Montési 2013), is near vertical or dipping to the northeast. In the Southern California Earthquake Center Community Fault Model (SCEC-CFM5.2, Nicholson *et al.* 2017), it is mapped as a vertical fault in the Coachella Valley (Fig. 1a). In contrast, analyses of interseismic strain fields (Fialko 2006; Tymofeyeva *et al.* 2019) and potential field data (Fuis *et al.* 2012, 2017; Langenheim & Fuis 2022) point to a northeast dipping SSAF similar to its neighbouring strand in San Gorgonio Pass (SGP, Fig. 1a), the latter being well constrained by small to moderate sized events (Jones *et al.* 1986; Nicholson 1996). A deep northeast dipping SSAF is supported by more seismicity on that

<sup>†</sup>Now at: College of Earth, Ocean, and Atmospheric Sciences, Oregon State University, Corvallis, OR, USA.

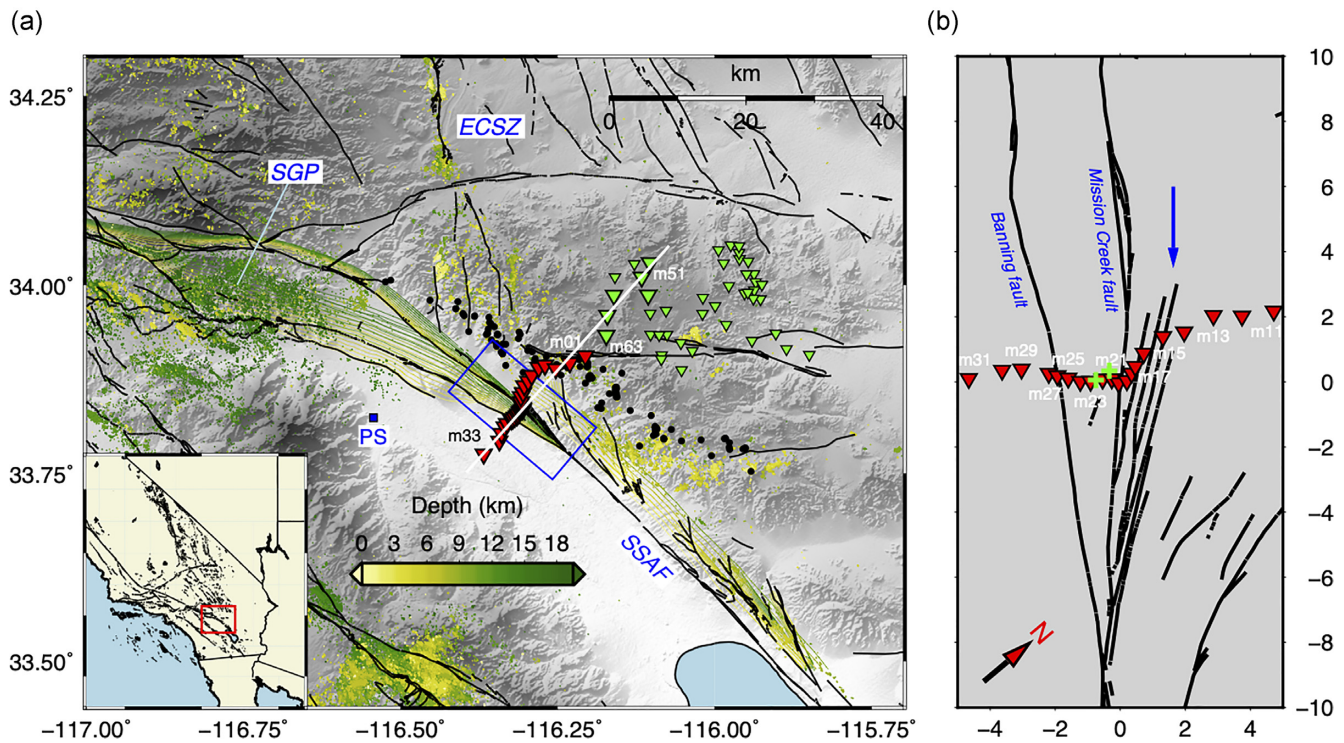


**Figure 1.** Study area in the context of the SSAF. (a) Fault traces at the surface (black lines) and contours along the SSAF planes from shallow (yellow) to 14 km depth (green) from the SCEC-CFM5.2 (see the text). The SSAF strand accommodating most of the plate boundary strain to the south is estimated to be vertical and has no contours. Secondary or ancestral faults are associated with the dipping structures (contours) to the northeast. MT stations acquired in 2019 (red) and in the Joshua Tree National Park during 2017–2018 (green) are depicted by triangles. Larger triangles show stations used in the 2-D inversion and the white line represents the inversion model transect in Fig. 4. Depth coloured dots are local earthquakes from the Ross *et al.* (2019) catalogue. Black dots are events illuminating a large bimaterial structure at depth. Note the relative lack of seismicity directly beneath the SSAF and especially near the study area. San Gorgonio Pass (SGP), the Eastern California Shear Zone (ECSZ) and the town of Palm Springs (PS) are shown for reference and the white to grey background colours represent high-resolution topography from Smith & Sandwell (1997). (b) Zoom-in of blue box in (a) showing the MT profile transecting the SSAF zone, which consists of the Banning, Mission Creek and other minor fault strands. The blue arrow shows the location of a large change in electric resistivity in the across-fault direction (same arrow appears in Figs 2–4). The Thousand Palms Oasis Preserve Visitor Center is located at the origin and the green crosses show the locations of two fluid samples taken from the oases.

side of the surface SSAF, and a large structure with a clear seismic velocity contrast (bimaterial interface) intersecting this seismicity (Fig. 1a, Share & Ben-Zion 2016). However, these features can also be attributed to secondary faults in the northeast (Fig. 1a, Nicholson *et al.* 2017). Much of our inability to resolve this fundamental question about deeper SSAF structure is owed to the general lack of abundant seismicity in the region (Ross *et al.* 2019), which is essential in delineating fault geometry (e.g. Magistrale & Sanders 1996; Carena *et al.* 2004) and is a key data set in high-resolution seismic imaging studies (e.g. Share *et al.* 2019). Thus, more studies using non-seismic geophysical tools are needed to help inform SSAF properties and its associated seismic risk.

Here, we use an established electromagnetic imaging method, namely magnetotelluric (MT, Cagnard 1953) soundings, that does not depend on seismicity (or paucity thereof as in the study region) as a source, to image for the first time the crustal electrical resistivity structure of the SSAF. MT is a passive geophysical tool that measures ubiquitous natural variations in the Earth's magnetic field and induced electric fields generated in the subsurface. Resistivity within the Earth is then derived from frequency-dependent transfer functions (the MT impedance tensor and tippers) between magnetic and electric fields.

MT data are preferentially sensitive to high conductivity (inverse of resistivity) regions within the Earth (Chave & Jones (2012, and

references therein). Relative to the deeper mantle, continental crust is electrically resistive (Schwarz 1990) except for anomalous regions where conductive materials (e.g. aqueous fluids, graphite and melts) form interconnected networks (e.g. Bahr 1997). Thus, active crustal fault zones are optimal targets for MT imaging, where damaged and deformed rocks create pathways for conductive fluids to percolate through the crust, and strain localization forms a mechanism to connect fluids within these weakened zones (Becken & Ritter 2012). Structure, damage and deformation need not always be symmetric about a fault core and interconnected fluids can be distributed asymmetrically with little fluid migration across impermeable faults (e.g. Caine *et al.* 1996; Bedrosian *et al.* 2004). MT has been successfully used to infer fault zone properties such as the amount of damage, fluid content, geometry and strain conditions in, for example, central California (e.g. Becken *et al.* 2011; Tietze & Ritter 2013), Japan (Ogawa & Honkura 2004; Yoshimura *et al.* 2009) and Turkey (Turkoglu *et al.* 2008). Despite these successes, MT has yet to be broadly applied in southern California.

In this study, we apply MT imaging to a section of the SSAF in northern Coachella Valley near the Thousand Palms Oasis Preserve and where the Mission Creek and Banning fault strands merge (Fig. 1b). Despite ongoing debate over which strand is more active at present, both are well located at the study site using offsets in landforms and lithology and trenching data (e.g. Fumal *et al.* 2002;

Blisniuk *et al.* 2021). Near the surface, these strands together with other minor faults comprise a  $\sim$ 3 km wide SSAF zone embedded in Pliocene and Pleistocene stratified rock with Coachella Valley Quaternary sediments to the southwest (up to  $\sim$ 2 km thick in the central Valley, Ajala *et al.* 2019), thinner sediments immediately northeast of the Mission Creek strand and the Little San Bernardino Mountains (pre-Cenozoic metamorphic and crystalline rocks) outcropping  $\sim$ 10 km farther northeast (Rymer 2000). The presence of several oases in the area indicates a fault zone acting as a conduit and/or barrier for aqueous fluid flow (Catchings *et al.* 2009), making it an attractive MT target. We collected data in 2019 along a linear array transecting the SSAF near the Preserve and supplemented these with stations from a neighbouring array located in the Joshua Tree National Park (Fig. 1a) to image electric resistivities in the area. The seismicity to the northeast is  $\sim$ 10 km from the Preserve and located at 4–11 km depth (Fig. 1a). Analysing MT data that span the SSAF zone and a significant area to the northeast allows us to investigate fault zone resistivities and its connection to local seismicity.

## 2 DATA AND METHODS

The MT imaging was based on  $\sim$ 1-d long recordings of natural variations in Earth's electromagnetic field at 27 sites crossing the SSAF in 2019 and 6 sites installed in Joshua Tree in 2018 (Fig. 1a). These sites were acquired using the Zonge International 32-bit ZEN data logger with ANT-4 magnetic induction coils and Borin Ag-AgCl electrodes with 50 m dipoles. The ZEN was programmed to record at 256 samples per second (sps) for 8 hr followed by a burst of 4096 sps recording for 10 min. This sequence repeated several times within the  $\sim$ 1-d recording windows. Accompanying the 2019 survey was a magnetic remote reference installed at a low-noise site in the Borrego Desert ( $33.271608^\circ$  N  $116.064469^\circ$  W,  $\sim$ 66 km away). This site consisted of a Scripps marine data logger (Constable 2013) to which a GPS clock had been added, collecting data from two EMI-BF4 induction coils oriented north–south and east–west. Magnetic north was used for orientation during all installations. These recorded continuously at 500 sps for the duration of the weeklong survey. Given the depths and scale of investigation in this study and that  $> 500$  sps data did not exist for the remote reference site, we excluded the 4096 sps ZEN data from further analysis. To better limit very near-surface properties in the absence of these high-frequency data, water samples from the local oases were collected (Fig. 1b) and their resistivities were measured using a laboratory 4-electrode setup. Both samples had similar measured resistivities of  $6.2 \Omega\text{-m}$  ( $18.6^\circ\text{C}$ ) and  $5.9 \Omega\text{-m}$  ( $18.5^\circ\text{C}$ ). Finally, for uniformity, all ZEN data were upsampled to 500 sps and reformatted to conform to the Scripps marine data format.

Next, recorded time-series were inspected and trimmed where needed to remove times with spurious noise. The time-series were then transformed to the frequency domain and the frequency coefficients of all stations overlapping in time (including the remote reference) were processed with the code of Egbert (1997) to produce robust MT impedances and induction vectors/tippers (Parkinson 1959). The 500 sps data and the recording period of  $\sim$ 1 d allowed reliable responses to be computed within the  $\sim$ 0.01–2000 s range. The use of the Borrego Desert remote reference significantly improved data quality for some sites.

Following visual inspection of the calculated impedances and tippers, 20 per cent of the impedance data and 16 per cent of the tipper data were considered outliers and removed (Fig. 2a). The

outliers were generally associated with longest periods (fewer data points per period) and southwestern most stations located near the central Coachella Valley where cultural noise was most pronounced (Fig. 2a). This noise affected the electric field recordings more than the magnetic field; thus, tipper data existed at several southwest stations/periods where impedances were otherwise unreliable.

Given the linear nature of the MT array aligned in a southwest–northeast direction where most fault zone structural changes are expected, and the large topographic gradient in the area (22–1,495 m), we inverted the responses using the MARE2DEM 2-D finite-element algorithm with adaptive meshing that accommodates well irregular topography (Key 2016). Prior to inversion, an appropriate strike angle was determined through analyses of the tipper azimuths and phase tensors (Caldwell *et al.* 2004).

## 3 DATA ANALYSIS

Frequency-dependent phase tensors and tippers provide indicators of the structural characteristics in the area (Fig. 2, and Fig. S1, Supporting Information). Around the Mission Creek strand and shallow depths ( $< 1$  s) structure is predominantly 1-D, as evidenced by the near-circular phase tensors and relatively small tippers. This near surface region probably consists of a shallow layer(s) of damage rock and unconsolidated sediments characteristic of an active fault zone (Blisniuk *et al.* 2021; Share *et al.* 2022). After rotating the local coordinate system to the average strike of the Banning and Mission Creek strands ( $130^\circ/310^\circ$  E of N, Fig. 1b), the properties of the phase tensor ellipses and tippers show that fault zone geoelectric structures mostly align with fault orientation. At periods  $\sim$ 1–50 s around the Mission Creek strand, the phase tensors become elliptical, have  $< 5^\circ$  beta angles and uniformly align with average fault strike (median strike/alpha =  $322^\circ$ , Fig. 2b, top). These properties highlight 2-D dimensionality at upper- to mid-crustal depths with geoelectric strike near parallel to average fault strike. This is corroborated by a  $\sim$ 90° flip in beta  $< 5^\circ$  phase tensor orientations (median strike/alpha =  $25^\circ$ , Fig. 2b, top) northeast of stations m14–15 (arrow in Figs 1b and 2a), an indication that a prominent fault parallel electric interface has been crossed and the mode with largest phase has flipped from transverse magnetic (TM, southwest conductive side) to transverse electric (TE, northeast resistive side; Fig. 3). Along the entire profile and for periods up to 50 s, the largest tippers (real part) align with the fault normal (median azimuth =  $42^\circ/222^\circ$  E of N, Fig. 2b, bottom), further evidence of geoelectric strike approximating fault strike. Moreover, the tippers point (Parkinson convention, Parkinson 1959) toward a region of high conductivity within the SSAF zone (Fig. 2a), most likely related to a fluid-rich region of deformation and damage with the sharp electric contrast around stations m14–15 representing its northeastern edge. At periods  $> 10$  s, beta angles start to increase for impedances recorded in the southwest, which may indicate 3-D structure but also reflects the noisy nature of these data. Across the array there is a progressive rotation of phase tensor ellipses and tippers at long periods away from average fault strike (or the fault normal), revealing a prominent plate boundary conductor to the northeast (Fig. S1, Supporting Information). This rotation starts at lower periods ( $\sim$ 5 s) for northeast stations, highlighting again a resistive region with larger skin depth compared to the conductive fault zone. It also causes a median strike angle of  $15^\circ$  less than the fault normal for stations in the northeast (Fig. 2b, top). Taken together, the median of all phase tensor strike (alpha) and real tipper angles up to a period of  $\sim$ 50 s (Fig. 2b) defines a coordinate system with  $X = 311.4^\circ$  (along fault)

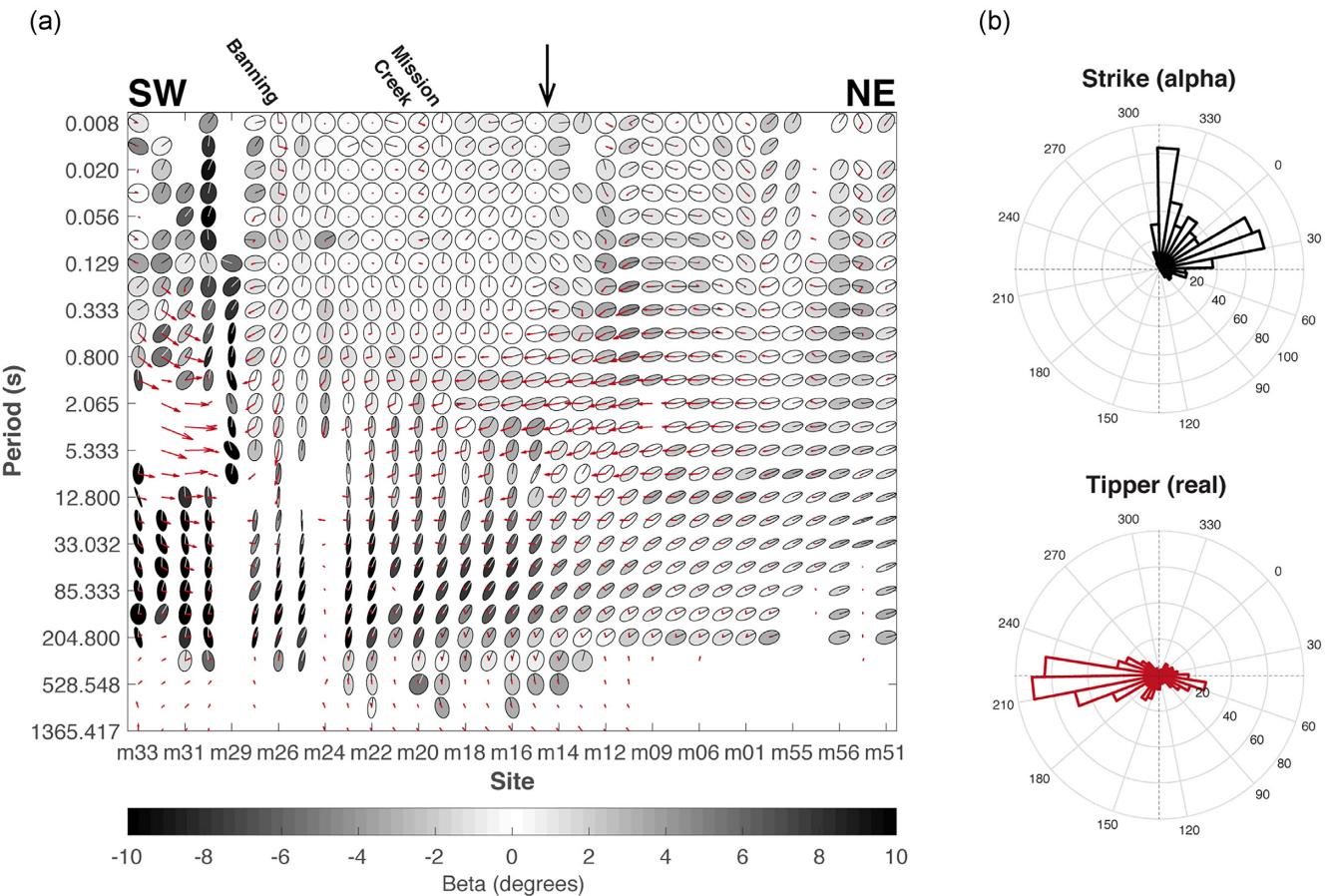


**Figure 2.** Phase tensor and tipper results. (a) Phase tensor ellipses and real tipper vectors (maroon arrows, Parkinson convention) of all data after outliers (gaps) were removed. The degree of ellipticity equals the difference between Phi-min and Phi-max, the black lines inside ellipses point to calculated strike ( $\alpha$ ) and the orientation of the major axes of ellipses relative to strike and the shading of the ellipses equals beta. The coordinate frame is the same as in Fig. 1(b). (b) Histograms of strike (top) and real tipper azimuths (bottom) for data up to 50 s. The dashed lines show the coordinate frame used [same as in (a)].

and  $Y = 41.4^\circ$  (across fault). Consequently, the impedances and tippers were rotated and  $> 50$  s data excluded from 2-D modelling as these express 3-D features.

#### 4 2-D INVERSION

In pseudo-sections of the rotated data (Fig. 3a), a broad region of high conductivity encompasses the SSAF zone, with average resistivities to the southwest and highest resistivities beneath stations to the northeast. To properly image the area and delineate SSAF structures, we inverted these data using MARE2DEM. The inversion model space consisted of a  $\sim 37$  km long surface profile with the Mission Creek strand/Thousand Palms Oasis at  $Y = 0$  km (Fig. 4) that included local high-resolution topography (from Smith & Sandwell 1997) and onto which the 33 station locations were projected. Beyond this  $\sim 37$  km profile, topography was set to be flat and extended from  $Y = -1000$  to  $1000$  km. We fixed the resistivity of the air above the surface to  $100\,000 \Omega \cdot \text{m}$  and beneath the surface the initial value was set to  $100 \Omega \cdot \text{m}$ . The latter extended down to a depth of  $1000$  km. From the surface to  $\sim 500$  m depth beneath the stations the inversion mesh triangles had a target length of  $200$  m (see Key 2016, for details). Given the dense station spacing (Fig. 1b) and expected high conductivities of an active fault zone (Fig. 3a), we assigned a target length of  $500$  m to the mesh from  $Y = -5$  to  $+5$  km and down to  $5$  km depth. Outside that zone

and down to  $10$  km depth the target length was  $1$  km, which then gradually increased to  $5$  km at  $50$  km depth and  $100$  km on either side of the  $37$  km profile. Beyond that, the mesh triangles increased without a specified target length to the edges of the model space.

The impedances and tippers of all except the five southwestern most stations were assigned error floors of  $10$  per cent and  $0.02$ , respectively. To the noisier and likely 3-D data in the southwest (Fig. 2a), we assigned error floors of  $15$  per cent and  $0.03$ . To test the resolution capabilities of these data plus errors, we constructed synthetic tests using hypothetical fault models, data calculated at the same periods and locations as the recorded data, and the same inversion mesh (Fig. S2, Supporting Information). The test cases all included a  $10 \Omega \cdot \text{m}$   $2$  km wide fault zone but with attitudes varying from a vertical fault zone to one with a shallow dip of  $30^\circ$  to the northeast (Fig. S2, Supporting Information). By keeping the fault zone width and resistivity constant these tests demonstrate the variable lateral and depth resolutions of the data and methodology. The resultant inversions (Fig. S2, Supporting Information) after adding Gaussian noise to the synthetic data suggest the recorded data are well suited to distinguish between these different fault zone geometries.

Next, inversions of the recorded data were completed with MARE2DEM. A target misfit of  $\text{rms} = 1$  was set at the start of the inversion and a horizontal to vertical smoothing ratio of  $0.5$  was selected to highlight expected vertical fault related features (Fig. S2,

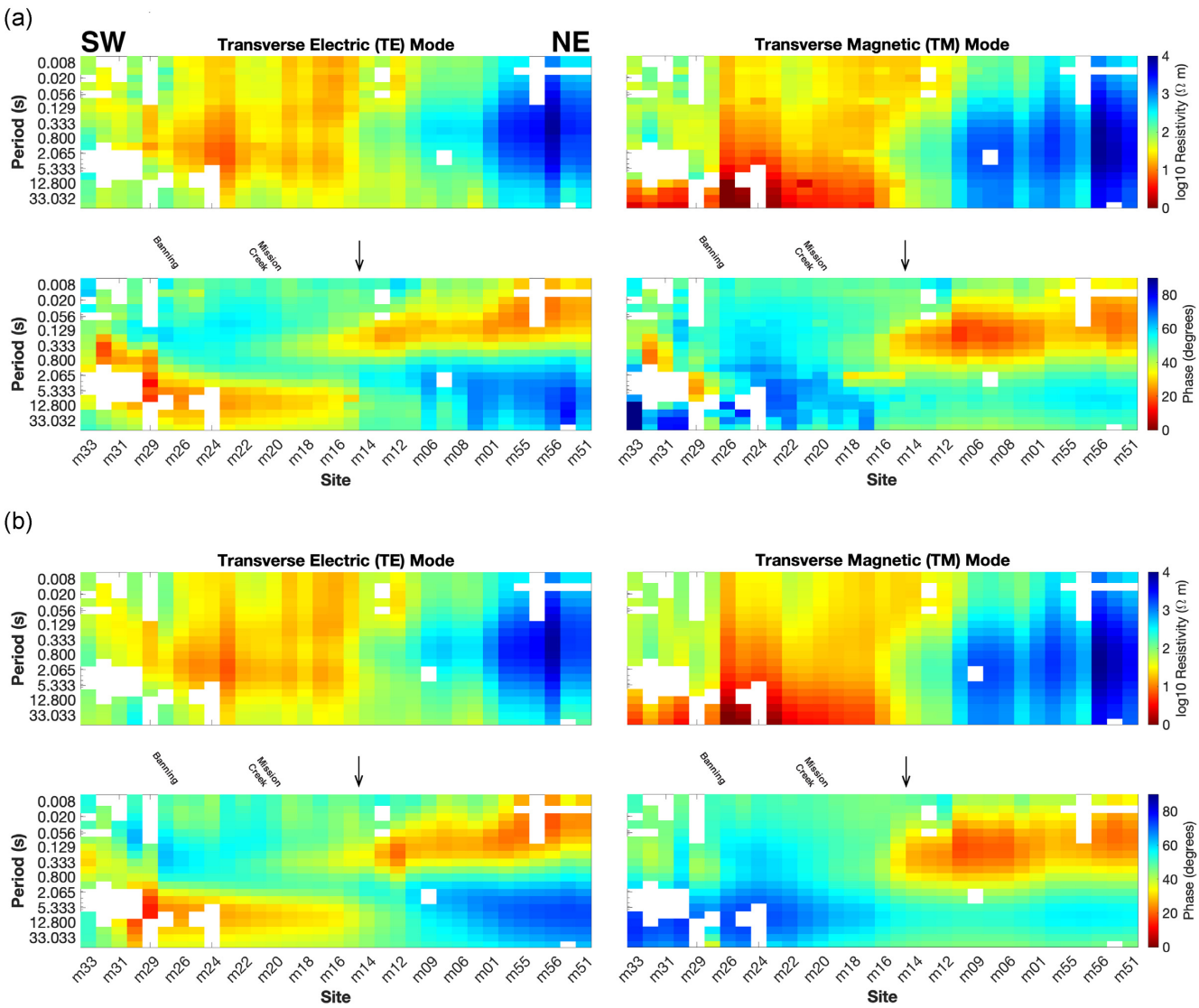


**Figure 3.** Pseudo-sections for the TE (left) and TM (right) modes up to 50 s period associated with recorded (a) and modelled (b) data responses. The modelled data correspond to the inverted model in Fig. 4. Differences between (a) and (b) are also illustrated in Fig. S3 (Supporting Information).

Supporting Information). The MARE2DEM algorithm attempts to reach the target misfit as fast as possible and then afterwards determines the smoothest model at that misfit (see Key 2016). With regard to the correction for static shifts caused by shallow small-scale features and irregular topography (e.g. Jiracek 1990), a traditional approach is to inspect the data and note which stations have parallel but offset TE and TM apparent resistivities at high frequencies, and to incorporate static shifts for those stations during inversion. This approach was challenged in our study region by the heterogeneous near surface of the SSAF zone that caused distorting effects other than, and in addition to, static shifts and because some sites had noisy and inaccurate high-frequency data (e.g. in the southwest, Fig. 2a). We instead employed the following systematic approach that leveraged the finite-element nature of MARE2DEM and helped identify more sites with static shifts including ones that may have been missed using the traditional approach. The first inversion was run without inverting for static shifts. After a few iterations ( $\sim 5$ ), the inversion was stopped to inspect which of the sites may be affected by this phenomenon. These were identified as sites that had low misfits for TE and TM mode phases and relatively low misfits for TM

mode apparent resistivities but had a parallel shift between the TE mode apparent resistivity data and modelled responses. The latter is an advantage of the finite-element code, which allows small-scale near surface anomalies to be added along the irregular topography to help offset TM mode static shifts but cannot do the same for the TE mode. Of the 33 sites, 17 were identified in this manner as having static shifts. Inversion for static shifts was activated for the 17 sites and the inversion restarted with a homogenous  $100 \Omega \cdot \text{m}$  subsurface. From a starting rms = 9.6, the inversion achieved an rms = 1.65 after 13 iterations with only incremental improvements after that. Because the initial target of rms = 1 was not reached, the model obtained at rms = 1.65 was not necessarily the smoothest for that misfit. So, a new target misfit of rms = 1.65 was set and the model after 13 iterations was used as the new starting model, and the inversion restarted. After a total of 18 iterations, the smoothest model with an rms = 1.65 was obtained (Fig. 4). The difference between Figs 3(a) and (b), and the recorded versus modelled data plotted in Fig. S3 (Supporting Information) illustrate how this misfit maps to the different sites and periods. As a supplementary, we used this same approach to invert only the TM mode data

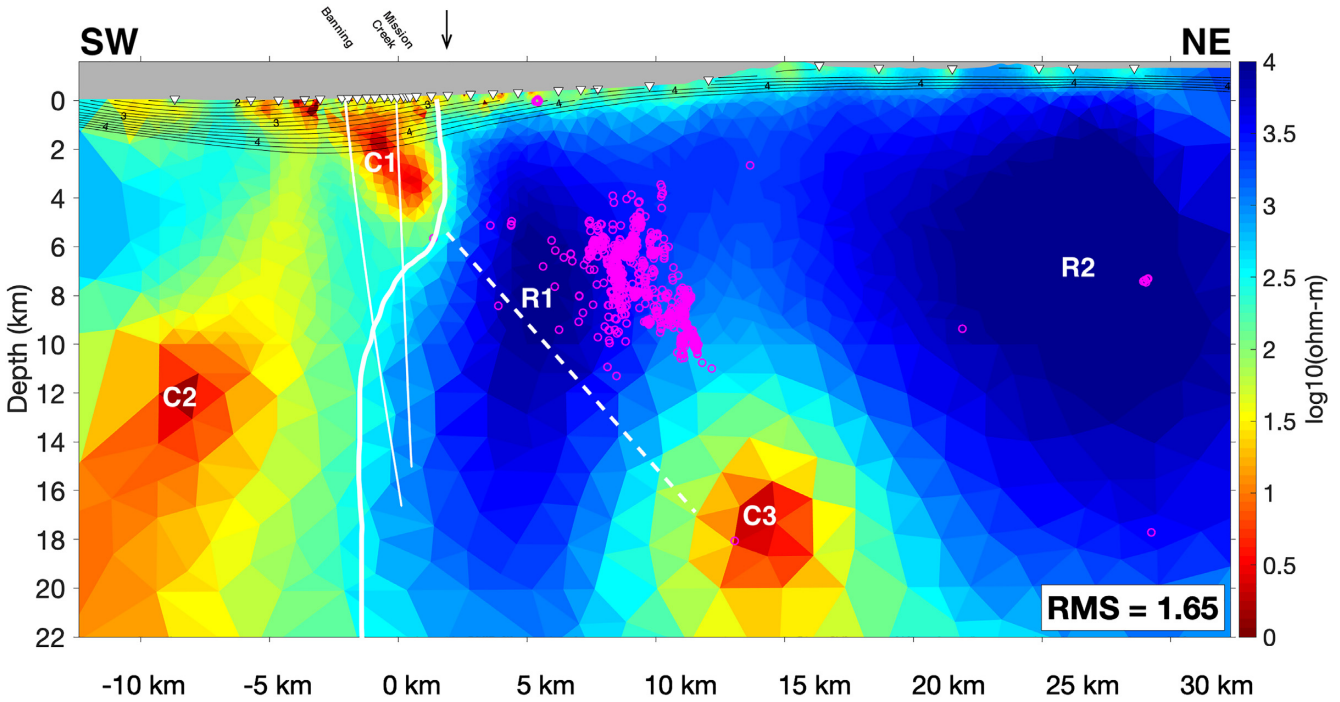


**Figure 4.** Final 2-D inverted model with prominent conductors (C1–C3) and resistors (R1–R2) marked. Magenta circles are local earthquakes within 3 km of this 2-D plane. The thick white line highlights a region of sharp resistivity change down to ~20 km depth and represents one (and most likely) interpretation for the location of the northeastern edge of the shallow SSAF zone and its near vertical geometry at greater depth. The nearby thinner white lines depict geometries of the Banning and Mission Creek strands from the SCEC-CFM5.2 (Fig. 1a). The dashed white line connecting C1 and C3 is an alternate interpretation of SSAF zone geometry at greater depth. Black contours are from the  $P$ -wave velocity model of Ajala *et al.* (2019) from 2 to  $4.4 \text{ km s}^{-1}$  sampled at increments of  $0.2 \text{ km s}^{-1}$  and highlights mostly basin geometry in the central Coachella Valley.

(Fig. S4, Supporting Information). These data have been shown to be less sensitive to 3-D effects (Wannamaker *et al.* 1984) and highly sensitive to sharp lateral changes in resistivity, thus highlighting across-fault structural changes in the study region.

Three crustal resistivity regions characterize the model in Fig. 4. First, a complex region of average to high conductivity (minima of  $\sim 1 \Omega\text{-m}$  at 2 and 12 km depth, C1 and C2) exists in the southwest and terminates at a sharp change in resistivity extending from  $\sim 2$  km northeast of the surface Mission Creek strand (e.g. Fig. S4, Supporting Information) to beneath the surface Banning strand in the ductile crust. The modelled values in this zone are comparable to those of the central San Andreas fault (Bedrosian *et al.* 2004; Becken *et al.* 2011). Second, the crust is mostly resistive northeast of this contrast reaching a maximum of  $\sim 10\,000 \Omega\text{-m}$  in places (R1 and R2). Finally, there exists a conductor, separate from C2, at  $> 13$  km depth beneath the most elevated part of the Little San Bernardino Mountains in the Joshua Tree National Park (C3). These features' general characteristics do not vary with changes in model smoothing or strike and the associated rotations of data responses (Fig. S5, Supporting Information).

Given that some regions in the model space are more poorly resolved than others, such as near surface areas with less station coverage, greater depths in general, and regions beneath conductors (e.g. Chave & Jones 2012), we applied a few conductance-preserving (conductivity-thickness product) alterations of C1–C3 to test if small changes in their properties are allowed without significantly affecting the misfit (i.e. changes within the nullspace, Munoz & Rath 2006). MT data are most sensitive to changes in conductance rather than conductivity, so by preserving conductance

these tests highlight how changes in the geometries and locations of C1–C3 affect data misfit. They also provide an indication of their relative influence on misfit and, therefore, the relative data sensitivity to these conductive parts of the model space. In general, the tests show that only small changes in C1–C3 are allowed without significantly increasing the model misfit (Fig. 5). Specifically, the steep northeast dipping geometry of anomaly C1 is well resolved as a more vertically orientated structure in the inverted model increases the rms to  $\sim 1.8$  (Fig. 5). And, the resistive region separating C2 and C3 is similarly well resolved as extensions of either C2 or C3 towards the other lead to large increases in rms (Fig. 5). For example, extending C2 only 6 km to the northeast produces the same significant increase in rms as removing it from the inverted model altogether (Fig. 5).

The model in Fig. 4 is our preferred result as it is equally well constrained by TE, TM and tipper data (Fig. S3, Supporting Information) and the majority of that data at periods  $< 50$  s is 2-D in nature with a consistent near fault-parallel strike (Fig. 2). However, as noted in Section 3, even at  $< 50$  s some stations and periods exhibit 3-D characteristics such as the northeastern most sites, for example (Fig. 2). To test the effects of these minor 3-D features in a predominantly 2-D upper- to mid-crustal region, we additionally applied a 2-D determinant inversion (Pedersen & Engels 2005; Wang *et al.* 2020; 2021). This type of inversion has been shown to produce a less-distorted 2-D model representations of a predominantly 2-D region that also includes 3-D structures (Wang *et al.* 2020). However, this lower distortion comes at the cost of larger model smoothness. The algorithm employed is embedded in the MARE2DEM package, which facilitates comparison with Fig. 4.

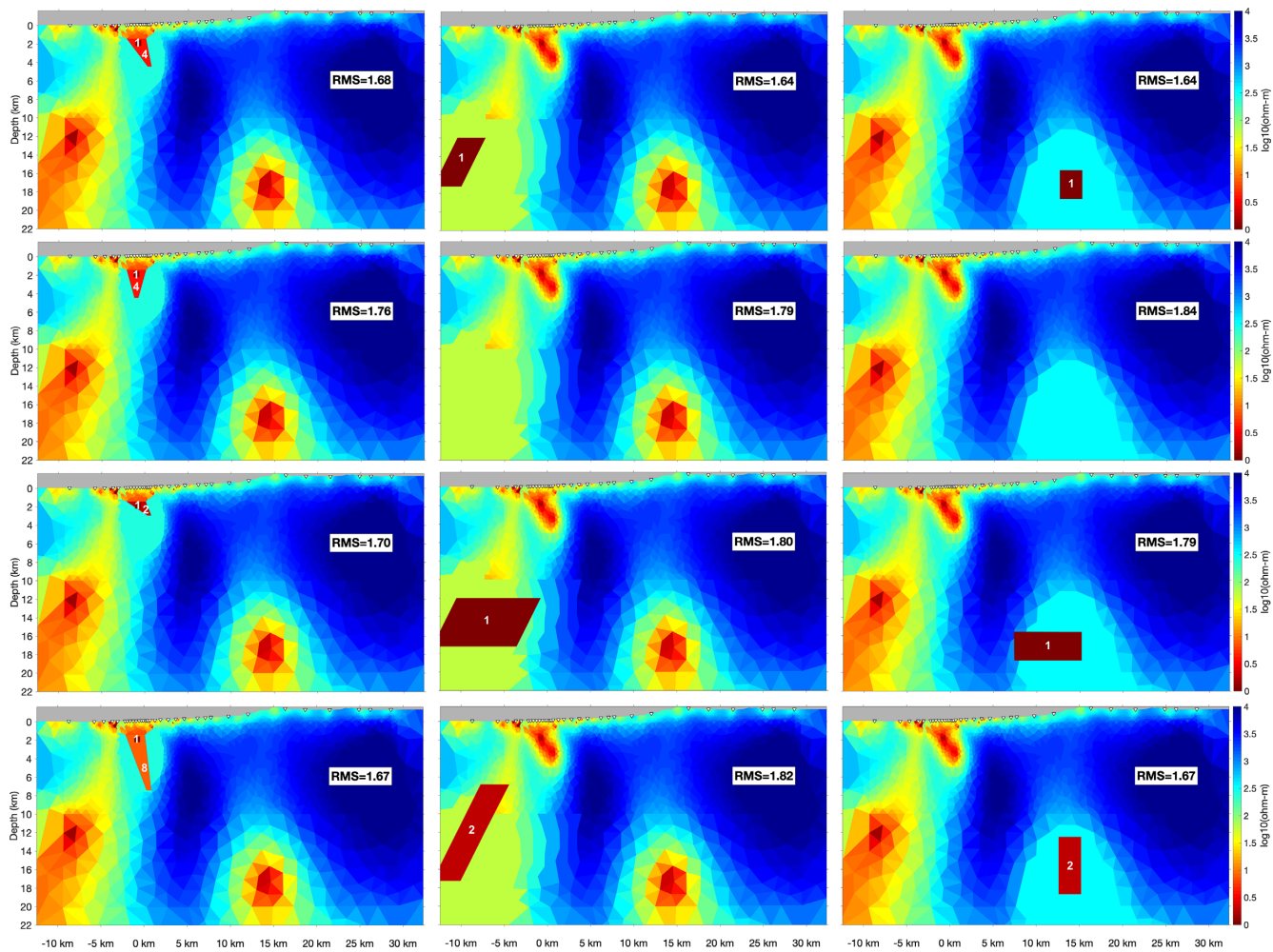


**Figure 5.** Equivalent resistivity anomaly representations of conductors C1 (left-hand column), C2 (middle column) and C3 (right-hand column) with similar misfits as in Fig. 4 (top row). Lower panels show removals, extensions and translations of these anomalies (all subsequent rows), and the misfits associated with those alterations. Numbers inside anomalies represent resistivities in  $\Omega\text{-m}$ .

During inversion, we used the same impedance tensor data (but multiplied to produce determinants), matching errors, and the model and inversion settings described above. Overall, all our resultant determinant inversion models were consistent with Fig. 4. In fact, even when we included data from all available periods, which constituted a significant increase in 3-D data, the determinant inversion result was still comparable to Fig. 4 (Figs S6 and S7, Supporting Information). In Fig. S6 (Supporting Information), anomalies C1–C3 and R1–R2 are all present but C2 is more conductive and extends to shallower depths, and the region containing R1, R2 and C3 is generally smoother with R1–R2 lower in resistivity and C3 smeared towards the northeast where there is less station coverage and the data are more 3D (Fig. 2, and Fig. S1, Supporting Information).

As a final reliability test on the inference of a mostly 2-D subsurface, a 3-D inversion was also carried out using all available data and with the ModEM finite-difference code (Kelbert *et al.* 2014). The features of the 3-D model were consistent with our 2-D inversions, but lacked the resolution of the MARE2DEM finite element code. These determinant and 3-D inversions demonstrate that our 2-D modelling approach applied to a limited data set is justified and features in the resultant 2-D model (Fig. 4) can be reliably interpreted.

## 5 DISCUSSION

Establishing properties related to structure and strain along the SSAF in Coachella Valley is essential for quantifying the potential magnitude and hazard of future large earthquakes. Fault geometrical irregularities play key roles in rupture propagation and subsequently earthquake magnitudes (e.g. Biasi & Wesnousky 2016). Rupture along dipping faults may have larger seismic moments because of the inherently larger slip area involved and can produce two to three times more ground shaking in the hangingwall compared to the footwall (Fialko 2006). Strain distributed on several neighbouring fault strands instead of a primary fault, influences the likelihood of multifault rupture and the extent of the resulting ground motion (Lozos 2016).

The results presented here provide insight into these topics as they relate to the SSAF in the northern Coachella Valley (Fig. 4). Anomaly C1 represents the broad SSAF zone ( $\sim 3$  km wide at the surface) in the upper crust. This near-surface width is corroborated by the presence of several anomalous fault damage-related structures within that same  $\sim 3$  km-wide zone as revealed by analysis of large-N seismic array data (Share *et al.* 2022). It extends to  $\sim 4$  km depth with largest amplitude at 2 km and locates northeast of the

central Coachella Valley, which implies its vertical to steep northeast dip is fault and not Valley basin controlled (Fig 4). If the Banning and Mission Creek strands predominantly constrain C1's geometry, then they likely have similar vertical to northeast dips at upper crustal depths (Catchings *et al.* 2009; Chi *et al.* 2021; Langenheim & Fuis 2022). The emergence of conductor C2 at depths  $> 10$  km is attributed to the transition from brittle to ductile behaviour in the area (Magistrale 2002; Smith-Konter *et al.* 2011) and a change in pore-space geometry as deep creep causes minute amounts of migrating fluid to become trapped and highly interconnected (Gough 1986; Park *et al.* 1992; Wannamaker *et al.* 2008). These deep fluids are likely sourced from the dehydrating metasediments and/or Peninsular Ranges batholith underlying the Coachella Valley sediments. The modelled location of C2 5–10 km southwest of the surface Mission Creek strand has some uncertainty, because of limited station coverage on that side. In contrast, greater station coverage northeast of the Mission Creek results in lower uncertainty and better model resolution and the data do not require C2 to extend significantly in that direction (Figs 5, and Fig. S4, Supporting Information). Instead, resistor R1 fits the data best and extends near vertically down to  $\sim 20$  km depth. The high resistivities of R1 suggest relatively dry hard rock, most likely crystalline basement (Catchings *et al.* 2009; Ajala *et al.* 2019), and in case these rocks do contain minor conductive materials, then those materials are not well interconnected and/or exist on such a small scale that they are poorly resolved. Most of the seismicity in this area locates within the more resistive parts of the model and is closer to conductor C3 than C1 or C2 (Figs 4, and Figs S4 and S6, Supporting Information). We propose C3 is a separate fluid or mineral rich creeping zone in the ductile crust that helps drive local earthquake activity in the more resistive and mechanically stronger crust above it. This correlation between small-scale brittle failure and high resistivity has been observed along minor faults in central California (Bedrosian *et al.* 2004), Japan (Ogawa & Honkura 2004), New Zealand (Wannamaker *et al.* 2009) and Turkey (Gurer & Bayrak 2007).

The uppermost 500 m of C1 has an average resistivity of  $35 \Omega\text{-m}$  (Fig. 4). Assuming the  $\sim 6 \Omega\text{-m}$  oases samples are representative of the type of fluids reducing the observed resistivities in the shallow fault zone (they interact and react with similar materials) and using Archie's (1942) law, gives porosity estimates of 18 per cent ( $n = 1$ , highly interconnected crack network) to 44 per cent ( $n = 2$ , partially connected pores) for the near surface. The decrease in the resistivity of C1 with depth (minimum of  $\sim 1 \Omega\text{-m}$  at 2 km depth) is attributed to decreased fluid resistivities and not porosity as that is expected to decrease with depth and therefore have a resistivity enhancing effect. We suggest two mechanisms driving the changes in fluid resistivity. The first is a rapid decrease in fluid resistivity expected in the upper crust due to temperature and pressure increases with depth, which can lead to more than an order of magnitude reduction (Nesbitt 1993). Second, because of the influx of fresh water from the surrounding creeks and mountains, the oases fluids represent an adequate but diluted (more resistive) proxy for the fluids present at 2 km depth in the fault zone. These two factors can result in a reduction of fluid resistivities to  $< 1 \Omega\text{-m}$  and produce the observed C1 minimum resistivity if well interconnected cracks with porosities of 10–15 per cent are assumed (e.g. Unsworth *et al.* 1997; Bedrosian *et al.* 2004). Note, this range represents an upper bound for porosity because, for example, the alteration of clays with increasing depth within the fault zone likely also reduces resistivity. In the mid-crust porosities decrease even further, the effects of increasing temperature and pressure become negligible (Nesbitt 1993) and observed resistivities are subsequently higher (bottom of C1). We do not have

direct bounds on the fluid and mineral properties producing deeper conductors C2 and C3. Others have suggested that lower crustal conductors in active tectonic settings with resistivities of  $\sim 1 \Omega\text{-m}$  only require porosities of 0.1–3 per cent if the highly interconnected *in situ* fluids have salinities exceeding that of seawater (e.g. Gough 1986; Hyndman *et al.* 1993; Becken & Ritter 2012). C2 and C3 (at least in part) are likely caused by similar mechanisms.

Taken together, the imaged anomalies (Fig. 4) and other geophysical inputs permit two interpretations for fault zone geometries and processes. The major strands of the SSAF zone in the upper crust are vertical to steeply northeast dipping and (1) evolve into a near vertical fault zone at greater depth that acts mostly as a barrier to northeast migration of fluids sourced in the southwest. A mature fault zone with a well-developed core but diminished damage and deformation zones (i.e. expected SSAF at mid-crustal depths) is likely to be impermeable (Caine *et al.* 1996). This type of impermeability and asymmetric distribution of crustal fluids about a major transform fault at depth have been observed along, for example, the central San Andreas and the Dead Sea Transform (Ritter *et al.* 2003; Bedrosian *et al.* 2004). In this interpretation, the seismicity in the northeast is therefore associated with secondary or ancestral faults (Fig. 1a) with small (<5 per cent) associated seismic velocity contrasts (Barak *et al.* 2015; Share & Ben-Zion 2016; Share *et al.* 2019). This is in line with the SCEC-CFM5.2 and high-resolution geophysical imaging of the same fault strands about 25 km to the northwest (Catchings *et al.* 2009). Or (2) the SSAF zone continues to dip northeast at greater depth, accommodates some of the local seismicity, manifests as C3 in the ductile crust but is either dry or consists of disconnected small-scale fluid-rich cracks from  $\sim 5$  to 13 km depth. These deeper characteristics (2) are not indicative of a mature and active transform fault that has probably experienced many large earthquake ruptures (Wesnousky 1990; Weldon *et al.* 2005). And, it requires an alternate explanation for the imaged near vertical crustal resistivity contrast near the surface SSAF zone that is not the active plate boundary. However, the second interpretation is consistent with estimates from geodetic (Fialko 2006; Lindsey & Fialko 2013; Tymofeyeva *et al.* 2019) and potential field (Fuis *et al.* 2012, 2017; Langenheim & Fuis 2022) data, the latter being most sensitive to structures at  $< 10$  km depth though.

An argument can be made for a non-simple broad deep SSAF zone that is a mix of (1) and (2), but that would require a lack of kilometre-scale localization of ductile fault roots (e.g. Montési 2013) driven by high crustal temperatures and low viscosities (Takeuchi & Fialko 2013). However, heat flow at the site is on par with well-localized fault systems, embedded in similar lithologies, to the north and west (Lachenbruch *et al.* 1985; Magistrale 2002) and it only starts increasing farther south, as does the observed shallow creep of the SSAF (Sieh & Williams 1990; Tymofeyeva *et al.* 2019). Moreover, the deep crustal conductors imaged in this study, inferred to represent ductile fault roots, are not connected but separated by well-resolved resistive crust (Figs 4 and 5, and Figs S5 and S6, Supporting Information).

## 6 CONCLUSIONS

Our results permit two interpretations of the electric SSAF zone. It is vertical to steeply northeast dipping in the upper crust and (1) is near vertical at greater depth creating mostly an impermeable barrier for northeast fluid migration or (2) continues to dip northeast but is anomalously dry and relatively resistive up to 13 km depth where it manifests as a secondary deep crustal conductor. The deeper near

vertical fault interpretation (1) is more likely as it is the simplest explanation for the observed anomalies and the active SSAF zone. It is also consistent with other major transform fault systems both in terms of resistivity and its complex shallow to simpler deeper fault zone nature. In any case, the general lack of seismicity and presence of shallow aseismic creep along parts of the Coachella Valley SSAF remain enigmatic. More insights from MT and other geophysical tools are required including joint inversions, which is beyond the scope of this focused study. Several new across-fault MT arrays to the southeast could help establish the along-strike continuity of anomalies C1–C3 and R1, respectively, and delineate changing fault zone widths, geometries, and their connection to seismicity, heat flow and creep. To the northwest more MT data could illuminate the conductive region identified at longer periods in Fig. 2(a) and Fig. S1 (Supporting Information) and its relation to regional tectonics.

## ACKNOWLEDGMENTS

We thank Deborah Rogers and Ginny Short (Center for Natural Lands Management and Thousand Palms Oasis Preserve), Brian Ousley (Bureau of Land Management), Tom Anderson, Chris Schoneman and Alicia Thomas (Sonny Bono Salton Sea National Wildlife Refuge), and Martin Alvarez (City of Palm Desert) for help with permitting and access to the field sites. We also acknowledge graduate students Hannah Peterson and Rosslyn King for their assistance during field work. We thank Kerry Key and Gary Egbert for their analysis codes, and Yuri Fialko, Rasheed Ajala and Victoria Langenheim for useful discussions. This work was supported by the Southern California Earthquake Center (SCEC) award no. 19200. P-ES was also supported by a Green Foundation Postdoctoral Fellowship (Institute of Geophysics and Planetary Physics/Scripps Institution of Oceanography). SW was funded by the Norwegian Research Council (294404, 309960 and 324442) and the National Infrastructure for High-Performance Computing and Data Storage in Norway (nn9872k). We thank the editors of GJI and numerous anonymous reviewers for their suggestions which led to improvements in the manuscript. We would especially like to acknowledge and thank the late Phil Wannamaker for his review and constructive comments on this paper, as well as a life of service and lasting impact on geophysics and geophysicists worldwide. Any use of trade, firm, or product names is for descriptive purposes only and does not imply endorsement by the U.S. Government.

## DATA AVAILABILITY

All data are publicly available (<https://doi.org/10.5066/P990U7GE>).

## REFERENCES

- Ajala, R., Persaud, P., Stock, J. M., Fuis, G. S., Hole, J. A., Goldman, M. R. & Scheirer, D. S., 2019. Three-dimensional basin and fault structure from a detailed seismic velocity model of Coachella Valley, Southern California, *J. geophys. Res.*, **124**(5), 4728–4750.
- Archie, G. E., 1942. The Electrical Resistivity Log as an Aid in Determining Some Reservoir Characteristics, *Trans. AIME*, **146**(01), 54–62.
- Bahr, K., 1997. Electrical anisotropy and conductivity distribution functions of fractal random networks and of the crust: the scale effect of connectivity, *Geophys. J. Int.*, **130**, 649–660.
- Barak, S., Klemperer, S. L. & Lawrence, J. F., 2015. San Andreas Fault dip, Peninsular Ranges mafic lower crust and partial melt in the Salton Trough, Southern California, from ambient-noise tomography, *Geochem. Geophys. Geosyst.*, **16**, 3946–3972.
- Becken, M. & Ritter, O., 2012. Magnetotelluric studies at the San Andreas Fault Zone: implications for the role of fluids, *Surv. Geophys.*, **33**(1), 65–105.
- Becken, M., Ritter, O., Bedrosian, P. A. & Weckmann, U., 2011. Correlation between deep fluids, tremor and creep along the central San Andreas Fault, *Nature*, **480**(7375), 87–90.
- Bedrosian, P. A., Unsworth, M. J., Egbert, G. D. & Thurber, C. H., 2004. Geophysical images of the creeping segment of the San Andreas Fault: implications for the role of crustal fluids in the earthquake process, *Tectonophysics*, **385**, 137–156.
- Biasi, G. P. & Wesnousky, S. G., 2016. Steps and gaps in ground ruptures: empirical bounds on rupture propagation, *Bull. seism. Soc. Am.*, **106**(3), 1110–1124.
- Blisniuk, K., Scharer, K., Sharp, W. D., Burgmann, R., Amos, C. & Rymer, M., 2021. A revised position for the primary strand of the Pleistocene-Holocene San Andreas fault in southern California, *Sci. Adv.*, **7**(13), eaaz5691, doi:[10.1126/sciadv.aaz5691](https://doi.org/10.1126/sciadv.aaz5691).
- Cagniard, L., 1953. Basic theory of the magneto-telluric method of geophysical prospecting, *Geophysics*, **18**, 605–635.
- Caine, J. S., Evans, J. P. & Forster, C. B., 1996. Fault zone architecture and permeability structure, *Geology*, **24**, 1025–1028.
- Caldwell, T. G., Bibby, H. M. & Brown, C., 2004. The magnetotelluric phase tensor, *Geophys. J. Int.*, **158**, 457–469.
- Carena, S., Suppe, J. & Kao, H., 2004. Lack of continuity of the San Andreas Fault in southern California: three-dimensional fault models and earthquake scenarios, *J. Geophys. Res.: Solid Earth*, **109**(B4), doi:[10.1029/2003JB002643](https://doi.org/10.1029/2003JB002643).
- Catchings, R. D., Rymer, M. J., Goldman, M. R. & Gandhok, G., 2009. San Andreas fault geometry at desert hot springs, California, and its effects on earthquake hazards and groundwater, *Bull. seism. Soc. Am.*, **99**(4), 2190–2207.
- Chave, A. D. & Jones, A. G.(Eds.), 2012. *The Magnetotelluric Method: Theory and Practice*. Cambridge University Press. 552pp.
- Chi, B., Qiu, H., Share, P.-E., Vernon, F. L. & Ben-Zion, Y., 2021. Reverse-time migration of fault zone reflected waves: methodology and application to the Southern San Andreas fault, *Seismol. Res. Lett.*, **92**(2B), 1422, doi:[10.1785/0220210025](https://doi.org/10.1785/0220210025).
- Constable, S., 2013. Review paper: instrumentation for marine magnetotelluric and controlled source electromagnetic sounding, *Geophys. Prospect.*, **61**(s1), 505–532.
- Egbert, G. D., 1997. Robust multiple-station magnetotelluric data processing, *Geophys. J. Int.*, **130**, 475–496.
- Fialko, Y., 2006. Interseismic strain accumulation and the earthquake potential on the southern San Andreas fault system, *Nature*, **441**(7096), 968–971.
- Fuis, G. S., Scheirer, D. S., Langenheim, V. E. & Kohler, M. D., 2012. A new perspective on the geometry of the San Andreas fault in southern California and its relationship to lithospheric structure, *Bull. seism. Soc. Am.*, **102**(1), 236–251.
- Fuis, G. S. et al., 2017. Subsurface geometry of the San Andreas Fault in Southern California: results from the Salton Seismic Imaging Project (SSIP) and strong ground motion expectations, *Bull. seism. Soc. Am.*, **107**(3), 1642–1662.
- Fumal, T. E., Rymer, M. J. & Seitz, G. G., 2002. Timing of Large Earthquakes since A.D. 800 on the Mission Creek Strand of the San Andreas Fault Zone at Thousand Palms Oasis, near Palm Springs, California, *Bull. seism. Soc. Am.*, **92**(7), 2841–2860.
- Gough, D. I., 1986. Seismic reflectors, conductivity, water and stress in the continental crust, *Nature*, **323**, 143–144.
- Gurer, A. & Bayrak, M., 2007. Relation between electrical resistivity and earthquake generation in the crust of West Anatolia, Turkey, *Tectonophysics*, **445**, 49–65.
- Hyndman, R. D., Vanyan, L. L., Marquis, G. & Law, L. K., 1993. The origin of electrically conductive lower continental crust: saline water or graphite?, *Phys. Earth planet. Inter.*, **81**(1), 325–345.
- Jiracek, G. R., 1990. Near-surface and topographic distortions in electromagnetic induction, *Surv. Geophys.*, **11**(2), 163–203.

- Jones, L. M., Hutton, L. K., Given, D. D. & Allen, C. R., 1986. The North Palm Springs, California, earthquake sequence of July 1986, *Bull. seism. Soc. Am.*, **76**, 1830–1837.
- Kelbert, A., Meqbel, N., Egbert, G. D. & Tandon, K., 2014. ModEM: a modular system for inversion of electromagnetic geophysical data, *Comput. Geosci.*, **66**, 40–53.
- Key, K., 2016. MARE2DEM: a 2-D inversion code for controlled-source electromagnetic and magnetotelluric data, *Geophys. J. Int.*, **207**(1), 571–588.
- Lachenbruch, A. H., Sass, J. H. & Galanis, S. P., Jr., 1985. Heat flow in southernmost California and the origin of the Salton Trough, *J. geophys. Res.: Solid Earth*, **90**(B8), 6709–6736.
- Langenheim, V. E. & Fuis, G. S., 2022. Insights into the geometry and evolution of the southern San Andreas fault from geophysical data, southern California, *Geosphere*, **18**(2), 458–475.
- Lindsey, E. O. & Fialko, Y., 2013. Geodetic slip rates in the southern San Andreas Fault system: effects of elastic heterogeneity and fault geometry, *J. geophys. Res.*, **118**, 689–697.
- Lozos, J. C., 2016. A case for historic joint rupture of the San Andreas and San Jacinto faults, *Sci. Adv.*, **2**(3), e1500621, doi:10.1126/sciadv.1500621.
- Magistrale, H. & Sanders, C., 1996. Evidence from precise earthquake hypocenters for segmentation of the San Andreas fault in San Gorgonio Pass, *J. geophys. Res.*, **101**, 3031–3044.
- Magistrale, H., 2002. Relative contributions of crustal temperature and composition to controlling the depth of earthquakes in Southern California, *Geophys. Res. Lett.*, **29**(10), 1447, doi:10.1029/2001GL014375.
- Montési, L. G. J., 2013. Fabric development as the key for forming ductile shear zones and enabling plate tectonics, *J. Struct. Geol.*, **50**, 254–266.
- Muñoz, G. & Rath, V., 2006. Beyond smooth inversion: the use of nullspace projection for the exploration of non-uniqueness in MT, *Geophys. J. Int.*, **164**(2), 301–311.
- Nesbitt, B. E., 1993. Electrical resistivities of crustal fluids, *J. geophys. Res.*, **98**(B3), 4301–4310.
- Nicholson, C., 1996. Seismic behavior of the southern San Andreas fault zone in the northern Coachella Valley, California: comparison of the 1948 and 1986 earthquake sequences, *Bull. seism. Soc. Am.*, **86**, 1331–1349.
- Nicholson, C., Plesch, A. & Shaw, J.H., 2017. Community Fault Model Version 5.2: updating and expanding the CFM 3D fault set and its associated fault database, in *2017 SCEC Annual Meeting Proceedings & Abstracts*, **XXVII**, poster 234, pp. 142–143.
- Ogawa, Y. & Honkura, Y., 2004. Mid-crustal electrical conductors and their correlations to seismicity and deformation at Itoigawa-Shizuoka tectonic line, Central Japan, *Earth Planets Space*, **56**, 1285–1291.
- Park, S. K., Jiracek, G. R. & Johnson, K. M., 1992. Magnetotelluric evidence for a brittle-ductile transition, peninsular ranges batholith, southern California?, *Geophys. Res. Lett.*, **19**(21), 2143–2146.
- Parkinson, W. D., 1959. Directions of rapid geomagnetic fluctuations, *Geophys. J. R. astr. Soc.*, **2**(1), 1–14.
- Pedersen, L. B. & Engels, M., 2005. Routine 2D inversion of magnetotelluric data using the determinant of the impedance tensor, *Geophysics*, **70**(2), G33–G41.
- Ritter, O., Weckmann, U., Hoffmann-Rothe, A., Abueladas, A. & Garfunkel, Z., & DESERT Research Group, 2003. Geophysical images of the Dead Sea Transform in Jordan reveal an impermeable barrier for fluid flow, *Geophys. Res. Lett.*, **30**, doi:10.1029/2003GL017541.
- Roten, D., Olsen, K. B., Cui, Y. & Day, S. M., 2015. Quantification of fault zone plasticity effects with spontaneous rupture simulations, in *Best Practices in Physics-based Fault Rupture Models for Seismic Hazard Assessment of Nuclear Installations*, Vienna, Austria.
- Ross, Z. E., Trugman, D. T., Hauksson, E. & Shearer, P., 2019. Searching for hidden earthquakes in Southern California, *Science*, **364**(6442), 767–771.
- Rymer, M. J., 2000. Triggered surface slips in the Coachella Valley area associated with the 1992 Joshua Tree and Landers, California, Earthquakes, *Bull. seism. Soc. Am.*, **90**(4), 832–848.
- Schwarz, G., 1990. Electrical conductivity of the earth's crust and upper mantle, *Surv. Geophys.*, **11**, 133–161.
- Share, P.-E. & Ben-Zion, Y., 2016. Bimaterial interfaces in the South San Andreas Fault with opposite velocity contrasts NW and SE from San Gorgonio Pass, *Geophys. Res. Lett.*, **43**(20), 10680–10687.
- Share, P.-E., Guo, H., Thurber, C. H., Zhang, H. & Ben-Zion, Y., 2019. Seismic imaging of the Southern California plate-boundary around the South-Central Transverse Ranges using double-difference tomography, *Pure appl. Geophys.*, **176**(3), 1117–1143.
- Share, P., Qiu, H., Vernon, F. L., Allam, A. A., Fialko, Y. & Ben-Zion, Y., 2022. General Seismic Architecture of the Southern San Andreas Fault Zone around the Thousand Palms Oasis from a Large-N Nodal Array, *Seism. Record*, **2**(1), 50–58.
- Sieh, K. & Williams, P., 1990. Behavior of the southernmost San Andreas fault during the past 300 years, *J. geophys. Res.*, **95**, 6629–6645.
- Smith, W. H. F. & Sandwell, D. T., 1997. Global seafloor topography from satellite altimetry and ship depth soundings, *Science*, **277**, 1957–1962.
- Smith-Konter, B. R., Sandwell, D. T. & Shearer, P., 2011. Locking depths estimated from geodesy and seismology along the San Andreas Fault System: implication for seismic moment release, *J. geophys. Res.*, **116**, B06401, doi:10.1029/2010JB008117.
- Takeuchi, C. S. & Fialko, Y., 2013. On the effects of thermally weakened ductile shear zones on postseismic deformation, *J. geophys. Res.: Solid Earth*, **118**(12), 6295–6310.
- Tietze, K. & Ritter, O., 2013. Three-dimensional magnetotelluric inversion in practice—the electrical conductivity structure of the San Andreas Fault in Central California, *Geophys. J. Int.*, **195**(1), 130–147.
- Turkoglu, E., Unsworth, M., Caglar, I., Tuncer, V. & Avsar, U., 2008. Lithospheric structure of the Arabia-Eurasia collision zone in eastern Anatolia: magnetotelluric evidence for widespread weakening by fluids?, *Geology*, **36**, 619–622.
- Tymofeyeva, E. et al., 2019. Slow slip event on the southern San Andreas fault triggered by the 2017 MW8.2 Chiapas (Mexico) earthquake, *J. geophys. Res.*, **124**, B016765, doi:10.1029/2018JB016765.
- Unsworth, M. J., Malin, P. E., Egbert, G. D. & Booker, J. R., 1997. Internal structure of the San Andreas fault at Parkfield, California, *Geology*, **25**(4), 359–362.
- Wang, S., Constable, S., Reyes-Ortega, V., Jahandari, H., Farquharson, C. & Avilez-Esquivel, T., 2020. Two-dimensional determinant inversion of marine magnetotelluric data and a field example from the Gulf of California, Mexico, *Geophysics*, **86**, E37–E57.
- Wang, S., Constable, S., Rychert, C. A. & Harmon, N., 2021. A lithosphere–asthenosphere boundary and partial melt resolved using marine magnetotelluric data, **21**, doi:10.1029/2020GC009177.
- Wannamaker, P. E., Hohmann, G. W. & Ward, S. H., 1984. Magnetotelluric responses of three-dimensional bodies in layered earths, *Geophysics*, **49**(9), 1517–1533.
- Wannamaker, P. E. et al., 2008. Lithospheric dismemberment and magmatic processes of the Great Basin–Colorado Plateau transition, Utah, implied from magnetotellurics, *Geosyst. Geophys. Geochem.*, **9**, Q05019, doi:10.1029/2007GC001886.
- Wannamaker, P. E. et al., 2009. Fluid and deformation regime of an advancing subduction system at Marlborough, New Zealand, *Nature*, **460**(7256), 733–736.
- Weldon, R. J., Fumal, T. E., Biasi, G. P. & Scharer, K. M., 2005. Past and future earthquakes on the San Andreas fault, *Science*, **308**, 966–967.
- Wesnousky, S. G., 1990. Seismicity as a function of cumulative geologic offset: some observations from southern California, *Bull. seism. Soc. Am.*, **80**(5), 1374–1381.
- Yoshimura, R. et al., 2009. Magnetotelluric transect across the niigata-kobe tectonic zone, central Japan: a clear correlation between strain accumulation and resistivity structure, *Geophys. Res. Lett.*, **36**, L20311, doi:10.1029/2009GL040016.

## SUPPORTING INFORMATION

Supplementary data are available at [GJI](#) online.

**Figure S1.** Tipper induction arrows (real-maroon, imaginary-black) from Fig. 2(a) at periods of approximately 0.2, 2, 20 and 200 s plotted in map view. Note the rotation of real tippers away from the SSAF zone and towards a conductor in the northwest at longest periods.

**Figure S2.** Synthetic forward models (left) and recovered inverse solutions (right) using different fault zone geometries. The geometries are (top) a vertical fault zone anomaly extending from the Mission Creek fault strand surface location to 20 km depth embedded in a surrounding host rock with resistivity of 1000 W·m, (middle) same as (top) but for a fault zone with a constant dip of 30° to the northeast, and (bottom) similar resistivities again but a more geometrically complex fault zone that is vertical down to 6 km depth and starts to steeply dip to the northeast by 60° below that. The synthetic fault zone has a width of 2 km, a resistivity of 10 W·m and is embedded in a 1000 W·m host rock. The starting half-space used during inverse modeling had a resistivity of 100 W·m. The horizontal to vertical smoothing ratios used during inversion were 0.4 (top), 1.1 (middle) and 0.5 (bottom). Rms = 1 for all inverse solutions above.

**Figure S3.** Data (dots and circles) and responses (lines) from the final 2D model (Fig. 4) for TE (top, blue), TM (top, red) and TZY (across-fault) tippers (bottom, blue).

**Figure S4.** TM mode-only data inversion result of the across-fault profile in Figs 1(a) and 4. Same settings and procedure as in Fig. 4 were used to obtain this model but a lower misfit (rms = 1.41) was

achieved with this being the smoothest model at that misfit. TM mode data are less sensitive to 3-D effects and highlight sharp lateral changes in structure such as the northeastward flip from conductive to resistive crust starting at  $Y = 2\text{--}3$  km (arrow). Anomalies C1–C3 and R1–R2 are all observed but muted at depth because TM mode data are not sensitive to conductance. Symbols and references are the same as in Fig. 4 but the locations of C1–C3 and R1–R2 have changed.

**Figure S5.** (a) Inversion results using the same data as in Fig. 4, but for a horizontal to vertical smoothing ratio of 1 (left) and 2 (right). (b) Inversion results using the data in Fig. 4 but rotated to  $X = 306.4^\circ$  and  $Y = 36.4^\circ$ , and  $X = 316.4^\circ$  and  $Y = 46.4^\circ$  (right), respectively. All other parameters are the same as in Fig. 4 and all models have a final rms of 1.65.

**Figure S6.** 2-D determinant inversion result using all available data ( $>50$  s also). The determinant data were obtained by multiplying the TE and TM mode after rotation to the strike direction. Tipper data, by definition, were not included in the determinant inversion. This image represents the smoothest model at a target misfit of rms = 1. All references and symbols are in the same locations as in Fig. 4.

**Figure S7.** Pseudo-sections of the determinant data (all periods) associated with recorded (a) and modelled (b) responses. The modelled data correspond to the inverted model in Fig. S6.

Please note: Oxford University Press is not responsible for the content or functionality of any supporting materials supplied by the authors. Any queries (other than missing material) should be directed to the corresponding author for the paper.